Published in final edited form as:

Med Biol Eng Comput. 2018 February ; 56(2): 183–199. doi:10.1007/s11517-017-1770-3.

Automated breast tumor detection and segmentation with a novel computational framework of whole ultrasound images

Lei Liu[#1], **Kai Li**[#2], **Wenjian Qin**[#1,3], **Tiexiang Wen**[1], **Ling Li**[1], **Jia Wu**[4], and **Jia Gu**[1]

[1]Shenzhen Institutes of Advanced Technology, Chinese Academy of Sciences, Shenzhen 518055, People's Republic of China

[2]Department of Medical Ultrasonics, The Third Affiliated Hospital, Sun Yat-sen University, Guangzhou 510630, People's Republic of China

[3]University of Chinese Academy of Sciences, Beijing 100049, People's Republic of China

[4]Department of Radiation Oncology, Stanford University, Stanford, CA 94305, USA

[#] These authors contributed equally to this work.

Abstract

Due to the low contrast and ambiguous boundaries of the tumors in breast ultrasound (BUS) images, it is still a challenging task to automatically segment the breast tumors from the ultrasound. In this paper, we proposed a novel computational framework that can detect and segment breast lesions fully automatic in the whole ultrasound images. This framework includes several key components: preprocessing, contour initialization, and tumor segmentation. In the pre-processing step, we applied non-local low-rank (NLLR) filter to reduce the speckle noise. In contour initialization step, we cascaded a two-step Otsu-based adaptive thresholding (OBAT) algorithm with morphologic operations to effectively locate the tumor regions and initialize the tumor contours. Finally, given the initial tumor contours, the improved Chan-Vese model based on the ratio of exponentially weighted averages (CV-ROEWA) method was utilized. This pipeline was tested on a set of 61 breast ultrasound (BUS) images with diagnosed tumors. The experimental results in clinical ultrasound images prove the high accuracy and robustness of the proposed framework, indicating its potential applications in clinical practice.

Keywords

Ultrasound image; Breast; Automatic segmentation; Speckle reduction; Contour initialization; Level set segmentation

1 Introduction

Breast cancer is one of the high-incidence cancer types among women worldwide [1, 2]. Early detection of breast cancer is crucial for successful treatment and reducing the mortality rate [2]. Among existing diagnostic modalities, the biospecimenbased test remains the gold

Jia Wu jiawu@stanford.edu. Jia Gu jia.gu@siat.ac.cn.

standard to determine whether a breast lump is malignant or benign [3]. However, only around 10~31% of the breast lumps referred for surgical biopsy turn out to be malignant [3]. Most of the false positive biopsies are unnecessary and can be potentially avoided with a more reliable breast cancer screening technique. With the development of medical imaging techniques, magnetic resonance imaging (MRI), mammography, tomosynthesis, and ultrasound have been introduced in a clinical environment for the early detection of breast cancer. Compared to MRI, mammography, and tomosynthesis, breast ultrasound (BUS) imaging is a cost-effective and safe way for early cancer detection and diagnosis [4]. Segmentation of tumor regions in BUS is a key step with-in conventional computer-aided diagnosis (CAD) analysis, which aims to optimize the following treatment plan. In most centers, the segmentation of breast lesions is performed by manually tracing the lesion contours, where intra- and inter-rater variations are inevitable, which would confound the following analysis [4]. Hence, in order to achieve more effective and reproducible lesion contouring, automatic segmentation methods are required and become critical in many imaging-based applications such as computer-aided diagnosis and image-guided surgical planning. However, due to the speckle noise, the shadowing effect, and especially the low contrast between the lesion and its background, it remains a challenging task to accurately and robustly segment the breast tumor in BUS images.

A number of semiautomatic image segmentation methods have been investigated for breast tumor segmentation in BUS, such as the histogram thresholding [5, 6], the watershed transformation methods [7, 8], the clustering algorithms [9], the graph-based methods [10], the active contour models, and the level set algorithms [11, 12]. However, these methods require human interaction in the segmentation procedure, where the accuracy to some extent depends on the human observers.

In recent years, several fully automatic methods for breast tumor segmentation in BUS have been reported. Madabhushi and Metaxas [13] presented an automatic approach by combining empirical domain-specific knowledge with low- and high-level image features. Liu et al. [14] described a fully automatic segmentation method by using a well-trained texture classifier and an active contour model which combined the global statistical information and local edge information. Shan et al. [15] proposed an automatic segmentation for BUS images composing of three steps: region of interest (ROI) generation, multi-domain feature extraction, and classification using an artificial neural network.

In general, the available automatic segmentation schemes were usually divided into two steps: ROI identification and tumor segmentation [13–16]. The identification of ROI is usually based on pattern recognition techniques combining empirical domain knowledge of the lesions. The tumor segmentation is usually based on some classic segmentation methods, such as active contour model. However, all the parameters in those models have to be empirically predefined, and it easily results in segmentation failure because of the wrong ROI initialization when the true tumor is not located at the center of the image or the BUS image contrast is not obvious.

In this paper, we propose a fully automatic segmentation scheme for segmenting the tumor lesions in the whole BUS images. The contributions of our proposed algorithm are the

following: (1) a fully automatic contour initialization framework is proposed to automatically obtain the initial contour; (2) an improved Chan-Vese model based on the ratio of exponentially weighted averages (CV-ROEWA) model is proposed to refine the contours of the tumor regions accurately; (3) a new edge detector is proposed to make the proposed method more robust than the traditional gradient-based methods.

2 Methods

This section describes the scheme proposed for our automatic segmentation scheme of breast lesion in whole ultrasound images. Figure 1 summarizes graphically the different steps of the scheme, including the following:

1. Pre-processing, the non-local low-rank (NLLR) filter is firstly used to suppress the speckle noise and improve the visual quality of BUS images.
2. Contour initialization, an adaptive contour initialization framework based on Otsu-based adaptive thresholding (OBAT) pre-segmentation and morphologic operations to automatically locate the breast tumor regions.
3. Tumor segmentation, a novel CV-ROEWA model is proposed to further accurately refine the contours of the tumor regions.

In the following subsections, we will make the detailed description of the different steps of the procedure.

2.1 Pre-processing

It is well known that the ultrasound images often contain lots of speckle noise and artifacts which result in relatively low contrast and the signal to noise ratio (SNR). Therefore, a pre-processing procedure for speckle reduction is needed in advance so as to improve the performance of the subsequent segmentation.

Several filtering approaches have been proposed in the literature for reducing speckle in BUS images while preserving edge details. Among these methods, the most successful ones are those based on anisotropic diffusion and the bilateral filter [17]. Several existing speckle reduction schemes based on anisotropic diffusion are speckle reducing anisotropic diffusion (SRAD) [18, 22], interference-based speckle filtering followed by anisotropic diffusion (ISFAD) [19], anisotropic diffusion guided by Log-Gabor (ADLG) filters [20], fast feature-preserving speckle reduction via phase congruency (FFSRPC) [21], and NLLR [17].

Among the above speckle reduction filters, ADLG outperforms the ISFAD and SRAD compared with respect to real BUS images [20], FFSRPC outperforms ADLG [21], and NLLR performs better than FFSRPC [17]. In another word, NLLR can better maintain features with speckle removal than state-of-the-art methods. Based on the above consideration, NLLR is chosen to remove the speckle noise while preserving important features in BUS images.

In the following, we describe the NLLR filter.

The NLLR is a non-local low-rank filtering framework for speckle noise reduction. The windowed inherent variation (WIV) measure is employed to generate the guidance image, G, from the input image I as follows:

$$G(p) = \sqrt{\left|\Sigma_q g_{p,g} \bullet \left(\partial_x I\right)_q\right|^2 + \left|\Sigma_q g_{p,g} \bullet \left(\partial_y I\right)_q\right|^2} \quad (1)$$

where p is a pixel in I, q is a pixel in the rectangular neighborhood centered at p, and $g_{p,g}$ is a weighting function based on spatial affinity, which is defined as:

$$g_{p,q} \propto \exp\left(-\frac{dist_{p,q}}{2\sigma_w^2}\right) \quad (2)$$

where σ_w controls the spatial scale of the neighboring rectangle.

With the WIV-guidance image, the distance between two non-local patches centered at pixels p and q is computed as:

$$dist(p,q) = \left\|P_I(p) - P_I(q)\right\| \cdot \left\|P_G(p) - P_G(q)\right\| \quad (3)$$

where $\|\cdot\|$ represents the L_2 norm, and $P_I(p)$, $P_I(q)$, $P_G(p)$ and $P_G(q)$ are the vectorized patches centered at pixels p and q in image I and guidance image G, respectively. The K most similar patches for each patch are selected in the input image. In the implementation, the window for searching similar patches is $(2 \times S_w + 1) \times (2 \times S_w + 1)$ with $S_w = 20$ to reduce the computation time, $K = 30$ and patch size as 7×7.

After finding the K most similar patches $\{P_i\}_{i=1}^{K}$ (in the image I) for a given reference patch P_{ref}, a patch group (PG) matrix Ψ_I is constructed as:

$$\Psi_I = \left[V(P_{ref}),\ V(P_1),\ V(P_2),\ \cdots,\ V(P_K)\right] \quad (4)$$

where $V(.)$ vectorizes a patch as a 49-element column vector. Similarly, Ψ_D denotes the PG matrix for each pixel in the final despeckled image D. Due to the rank of Ψ_D which tends to be low and the rank of Ψ_I tends to be high, in the ultrasound images, a low-rank recovery process is formulated to estimate Ψ_D from Ψ_I. That is, Ψ_I is decomposed into a low-rank component (Ψ_D) and a spare component (Ψ_η) by solving:

$$\min_{\Psi_D,\ \Psi_\eta} \operatorname{rank}(\Psi_D) + \alpha\left\|\Psi_\eta\right\|_0 s.t.\ \Psi_I = \Psi_D + \Psi_\eta \quad (5)$$

where rank(Ψ_D) denotes the rank of Ψ_D, which equals to the L_0 norm of the singular values of Ψ_D; and a is a weight to balance the two regularization terms.

To better approximate the rank operator by combining the strength of the truncated nuclear norm and the weighted nuclear norm, a truncated and weighted nuclear norm (TWNN) $\|\cdot\|_{tw}$ is proposed:

$$\| \Psi_D \|_{tw} = \sum_{i=1}^{M} w_i \sigma_i(\Psi_D) \quad (6)$$

where M is the total number of the singular values; and w_i is the weight for the i-th singular value σ_i of ψ_D.

The w_i is defined as

$$w_i = \begin{cases} 0 & if\ i \le \lambda \\ \dfrac{\theta\sqrt{K+1}}{\sqrt{\sigma_i(\Psi_D) + \varepsilon}} & otherwise \end{cases} \quad (7)$$

where λ and θ are parameters, and ε is set to be 0.00001 to avoid division by zero. In all the experiments, $\lambda = 9$ and $\theta = 5\sqrt{2}$

And the initialization of $\sigma i(\Psi D)$ is

$$\sigma_i(\Psi_D) = \sqrt{\max\left(\sigma_i^2(\Psi_I) - \beta,\ 0\right)} \quad (8)$$

where β is a parameter that estimates the noise component.

The structured sparsity Ω_η is employed to approximate $\|\Psi_\eta\|_0$ for ultrasound speckle reduction, which is defined as:

$$\Omega_\eta = \sum_{g \in \Psi_\eta} \|g\|_\infty \quad (9)$$

where g is each 3 × 3 submatrix in Ψ_η; and $\|.\|_\infty$ is the maximum value over all the elements in g.

By putting the Eq. 6 and the Eq. 9 into Eq. 5, the final objective function to recover the underlying low-rank matrix is:

$$\min_{\Psi_D,\ \Psi_\eta} \sum_{i=1}^{M} w_i \sigma_i(\Psi_D) + \alpha \sum_{g \in \Psi_\eta} \|g\|_\infty s.t.\ \Psi_I = \Psi_D + \Psi_\eta \quad (10)$$

where α is set to be 1.0 in the current implementation.

The implementation also can be found in [17].

The phenomenon of speckle reduction by different filtering schemes is illustrated in Fig. 2 with two breast lesion ultrasound images.

2.2 Contour initialization

The initial contour detection is an important step to be considered prior to the segmentation process which based on active contour models. If the initial contour is outside the lesion area, the subsequent segmentation result would not be correct.

This stage yields the initial contours used in the subsequent segmentation steps by a set of simple but determinant operations in the proposed scheme. The flow chart of the proposed fully automatic contours initialization scheme is shown in Fig. 3.

Detailed procedures for this stage are given as follows:

2.2.1 Two-step OBAT pre-segmentation—Otsu method is a well-behaved automatic optimal global threshold selection method and has been widely used for its simplicity, low computational complexity, stability, and effectiveness [23]. However, when using the traditional Otsu method to separate the foreground object, most of the background is still retained in the segmentation results (see Fig. 4e–h). To solve this problem, a two-step OBAT method is proposed that constrains the search range of the ideal segmentation threshold to extract the foreground object inside the image.

A brief description of Otsu threshold method is presented below.

Supposed that the pixels of the gray image were expressed in L gray levels$[0, 1, \cdots, L-1]$, where the variable "L" refers to the total number of gray levels in the image, the number of pixels with gray level i is denoted as n_i and the total number of pixels can be expressed as $N = \sum_{i=0}^{L-1} n_i$. The probability density distribution of gray level i is denoted as $P_i = \frac{n_i}{N}$, and $\sum_{i=0}^{L-1} p_i = 1, p_i \geq 0$.

The pixels of the image can be divided into two classes C_0 (foreground) and C_1 (background) by a threshold t. Then, C_0 and C_1 respectively represent the pixels within $[0, 1, \cdots, t]$ and $[t+1, t+2, \cdots, L-1]$. The probabilities of the two classes and average can be denoted as

$$\omega_0 = \sum_{i=0}^{i=t} p_i, \qquad \omega_1 = \sum_{i=t+1}^{L-1} p_i \quad (11)$$

$$\mu_0 = \frac{1}{\omega_0(t)} \sum_{i=0}^{t} i p_i, \quad \mu_1 = \frac{1}{\omega_1(t)} \sum_{i=t+1}^{L-1} i p_i \quad (12)$$

The mean gray level values of the total image is computed as

$$\mu_T = \sum_{i=0}^{L-1} i p_i \quad (13)$$

The between-classes variance is defined as

$$\sigma_B^2 = \omega_0 (\mu_0 - \mu_T)^2 + \omega_1 (\mu_0 - \mu_T)^2 \quad (14)$$

Last, the optimal threshold t^* is chosen by maximizing σ_B^2.

$$t^* = \text{argmax} \sigma_B^2 \quad (15)$$

The experimental results with traditional Otsu algorithm indicate that the obtained threshold could not efficiently discriminate the lesion regions and normal tissues (see Fig. 4e–h).

To precisely separate the BUS image into background and foreground, we proposed a two-step OBAT method to search the ideal segmentation threshold for extracting the foreground object inside the BUS image.

The procedure of the proposed automatic threshold pre-segmentation is described as below:

1) Calculate the gray level L of the BUS image, where L refers to the total number of gray levels in the input image.

2) The traditional Otsu method is used to calculate the initial segmentation threshold t_1.

3) With the initial threshold t_1, the image I would be separated into two parts C_0 (foreground) and C_1 (background). In the BUS image, the gray levels of the pixels within this low echogenic tumor area are lower than surrounding. So,we assume the set C_0 implies the foreground object with a gray level of $[0, 1, \cdots, t]$, and C_1 represents the back-ground pixels with a gray level of $[t + 1, t + 2, \cdots, L - 1]$.

4) Retain the part C_0. The traditional Otsu method is used in the part C_0 to calculate the threshold t_2.

5) Segment the whole BUS image using threshold t_2.

2.2.2 Morphologic operations—There is also some fine noise which is some isolated misclassified regions in the binary images that generated by the two-step OBAT pre-segmentation, as shown in Fig. 5d. To reduce the impact of small misclassified regions, morphologic erosion and dilatation were performed, using a flat disk-shaped structuring element. In order to better separate the background and foreground, a 9-pixel-radius circular structuring element is performed in dilatation processing and a 3-pixel-radius circular structuring element is performed in erosion processing.

2.2.3 Fill the holes—A flood-fill operation is performed on the image to fill the holes inside the initial contour area of the segmented image.

2.2.4 Delete the border-connected regions—After the above operation, we find all the connected components. Each connected component represents a possible lesion region. It is assumed that the regions which directly connected with the border were not part of the lesion regions, often resulting from artifacts or shadows in the ultrasound exam [29]. The regions connected with the image borders were directly deleted in many kinds of literature, such as [29]. However, sometimes, the lesion region is also connected with the border. If we directly delete the border-connected regions, the lesion region will be also deleted. Therefore, we propose a criterion of the center window which is about one half size of the whole image and centered at the image center to eliminate false detected regions.

The criterion is as follows:

(1) If the border-connected region does not intersect with the center window, this border-connected region will be deleted from the lesion candidate list.

(2) If the border-connected region intersects with the center window, this border-connected region will be truncated by the center window.

2.2.5 The largest region discrimination—The connected region after primary segmentation based on threshold segmentation model through the above experiments may be more than one, but the real lesion area in the actual situation is often the largest area of the connected regions. So, an eight neighborhood tracking algorithm [30] is used to out-line the boundary of the lesion area and the size of lesion area as a basis for selecting the interested region. The largest connected region is chosen as the initial outline of the lesion.

Then, the preliminary contour is obtained by the above operations, as shown in Fig. 5.

The contour initialization could obtain a reliable lesion region, but it could not detect the boundaries of the tumor. For this reason, a post-segmentation stage is required to refine the tumor contour on the basis of the second contour initialization.

2.3 Tumor segmentation

After the initial contour has been identified, the next task is to accurately extract the boundaries of breast lesion using a suitable image segmentation approach. The CV model [24] as an active contour model based on Mumford-Shah segmentation techniques [26] and the level set method [27] is a very popular segmentation method for BUS images [25]. The CV model has the advantage that ensures the detected edge closed and continuous. Its disadvantages are that the initialization contours are required accurately and the reasonable energy function is difficult to obtain due to the BUS image quality. Due to the pseudo edges and noises, it tends to fall into the local minimum solution or generate boundary leakages. To solve this problem, a novel CV-ROEWA model is proposed.

Next, we first briefly review the traditional CV algorithm and, then, briefly review the ROEWA operator, followed by the discussion of the proposed CV-ROEWA model.

2.3.1 The CV model—The CV model is taken to refine the contour of the tumor regions by minimizing the energy functional $F(c_1, c_2, C)$, defined by

$$\begin{aligned} F(c_1, c_2, C) &= \mu \cdot Length(C) + \nu \cdot Area(inside(C)) \\ &+ \lambda_1 \int_{inside(C)} |I(x, y) - c_1|^2 dxdy \\ &+ \lambda_2 \int_{outside(C)} |I(x, y) - c_2|^2 dxdy \end{aligned} \quad (16)$$

where C is the evolving curve, $\mu \geq 0$, $\nu \geq 0$, $\lambda_1 > 0$, $\lambda_2 > 0$are fixed parameters, the constants c_1, c_2 depending on C are the averages of the image u_0 inside C and outside C, respectively. *Lenght(C)* denotes the length of the curve C and *Area(inside(C))* denotes the area of the region inside the curve C. This energy function can be represented by a level set formulation as follows:

$$\begin{aligned} F(c_1, c_2, \phi) &= \mu \int_\Omega \delta(\phi(x, y)) |\nabla \phi(x, y)| dxdy \\ &+ \nu \int_\Omega H(\phi(x, y)) dxdy \\ &+ \lambda_1 \int_\Omega |I(x, y) - c_1|^2 H(\phi(x, y)) dxdy \\ &+ \lambda_2 \int_\Omega |I(x, y) - c_2|^2 (1 - H(\phi(x, y))) dxdy \end{aligned} \quad (17)$$

where $H(\phi(x, y))$ denotes the Heaviside function, which is defined by

$$H(z) = \frac{1}{2} + \frac{1}{\pi} \cdot \arctan\left(\frac{z}{\varepsilon}\right) \quad (18)$$

Then, the energy minimization problem can be converted to solving a level set evolution equation. The energy $F(c_1, c_2, \phi)$ is minimized when ϕ is on the boundary of the object. Keeping c_1 and c_2 fixed and minimizing F, the equation in ϕ is

$$\frac{\partial \phi}{\partial t} = \delta_\varepsilon(\phi)\left[\mu \cdot div\left(\frac{\nabla \phi}{|\nabla \phi|}\right) - v - \lambda_1(u_0 - c_1)^2 + \lambda_2(u_0 - c_2)^2\right] \quad (19)$$

In (14)

$$\delta_\varepsilon(z) = \frac{d}{dz}H(z) = \frac{1}{\pi} \cdot \frac{\varepsilon}{\varepsilon^2 + z^2} \quad (20)$$

2.3.2 ROEWA operator—The ROEWA operator has constant false alarm rates and outstanding localization performance, which is proposed by Fjortoft et al. [28] for SAR images. The ROEWA operator is a line-by-line and column-by-column detector, which consists of computing the ratio of exponentially weighted averages on opposite sides of the central pixel in the horizontal and vertical directions.

To compute the horizontal edge strength component, the image $I(x, y)$ is first smoothed column by column using a linear minimum mean square error (MMSE) filter. In the discrete case, the MMSE filter f is implemented very efficiently by a pair of recursive filters $f_1(n)$ and $f_2(n)$, realizing the normalized causal and anti-causal part of $f(n)$, respectively

$$f_1(n) = a \cdot b^n u(n) \quad (21)$$

$$f_2(n) = a \cdot b^{-n} u(-n) \quad (22)$$

where $0 < b = e^{-\alpha} < 1$, $a = 1 - b$, and $u(n)$ are the discrete Heaviside function. The value of b is taken as 0.73. The smoothing function can be written as

$$f(n) = c \cdot b^{|n|} = \frac{1}{1 + b} f_1(n) + \frac{b}{1 + b} f_2(n - 1) \quad (23)$$

where $c = (1 - b)/(1 + b)$.

Next, the causal ($f_1(x), x > 0$) and anti-causal filter ($f_2(x), x 0$) are employed line by line with the result of the smoothing operation to obtain $\hat{\mu}_1(x)$ and $\hat{\mu}_2(x)$.

$$\hat{\mu}_{X1}(x, y) = f_1(x) * (f(y) \cdot I(x, y)) \quad (24)$$

$$\hat{\mu}_{X2}(x,\ y)\ =\ f_2(x) * (f(y) \cdot I(x,\ y)) \quad (25)$$

where $*$ denotes convolution in the horizontal direction and $\cdot$ denotes the convolution in the vertical direction. The vertical edge strength component $R_{Xmax}(x, y)$ is obtained in the same manner, except that the directions are interchanged.

$$\hat{\mu}_{Y1}(x,\ y)\ =\ f_1(y) \cdot (f(x) * I(x,\ y)) \quad (26)$$

$$\hat{\mu}_{Y2}(x,\ y)\ =\ f_2(y) \cdot (f(x) * I(x,\ y)) \quad (27)$$

The normalized ratio $R_{X\max}(x, y)$ is found by substituting $\hat{\mu}_{X1}(x-1, y)$ and $\hat{\mu}_{X2}(x+1, y)$ into the following:

$$\mathrm{R}_{\max}\ =\ \max\left\{ \frac{\hat{\mu}_1}{\hat{\mu}_2}, \frac{\hat{\mu}_2}{\hat{\mu}_1} \right\}. \quad (28)$$

Finally, with analogy to gradient-based edge detectors for optical images, the magnitude of the two components is

$$R(x, y)\ =\ \sqrt{R^2_{X\ \max}(x,\ y) + R^2_{Y\ \max}(x,\ y)} \quad (29)$$

The ROEWA-based edge detector is efficient for the detection of isolated step edges in speckled images. Figure 6 shows the gradient-based edge detectors and the ROEWA-based edge detectors for the same ultrasound image.

2.3.3 The CV-ROEWA model—In the traditional CV model which has been described above, the domain of the function $\delta_\varepsilon(\phi)$ is narrow, and this seriously suppressed the detection of the edges which are far away from the initial contours. In addition, it is difficult to find the accurate boundary of an object in low contrast images. To avoid boundary leakages or runs over ϕ, we construct an edge indicator function g as the curve evolution stop term to replace $\delta_\varepsilon(\phi)$. The role of the edge indicator function g is to make the dynamic curves move toward the object boundaries and make the evolution of the contour lines accurately stop at the boundary contour of the object. For this purpose, the edge indicator function can be defined as:

$$g(R)\ =\ e^{-\alpha \cdot (R/\beta)^2} \quad (30)$$

or

$$g(R) = \frac{1}{1 + (R/\beta)^2} \quad (31)$$

where R denotes the edge strength which obtained by ROEWA operator, and α and β are constants which are the coefficients of the speed function of the image edge strength field. The edge indicator function should be a monotone decreasing function, and it can move the zero level curve toward the object boundaries. Because the negative exponential form has better performance than the reciprocal form, the negative exponential form is chosen as the edge indicator function. Then, the corresponding evolution equation is

$$\begin{cases} \frac{\partial \phi}{\partial t} = g(R) \cdot \left[\mu \cdot div\left(\frac{\nabla \phi}{|\nabla \phi|} \right) - v - \lambda_1 (u_0 - c_1)^2 + \lambda_2 (u_0 - c_2)^2 \right] \\ \phi(0, x, y) = \phi_0(x, y) \qquad inside \quad of \quad \Omega \end{cases}, \quad (32)$$

In the implementation, the parameters are fixed as $\mu = 0.2$, $\nu = 0$, $\lambda_1 = 1.0$, $\lambda_2 = 1.0$, $\alpha = 0.2$, and $\beta = 0.2$.

2.4 Evaluation of the automatic segmentation scheme

To compute the difference between the Bground truth^ regions and automatically segmented regions, four quantitative performance measures of area error metrics are proposed in [29] including true positive (TP), false positive (FP), false negative (FN), and the Jaccard similarity (JS). They are defined as

$$TP = \frac{|\Omega_m \cap \Omega_a|}{|\Omega_m|} \quad (33)$$

$$FP = \frac{|\Omega_m \cup \Omega_a - \Omega_m|}{|\Omega_m|} \quad (34)$$

$$FN = \frac{|\Omega_a \cup \Omega_m - \Omega_a|}{|\Omega_m|} \quad (35)$$

$$JS = \frac{|\Omega_m \cap \Omega_a|}{|\Omega_m \cup \Omega_a|} \quad (36)$$

where Ω_m represents the area (number of pixels) of the manual tumor region delineated by an experienced radiologist, and Ω_a represents the area of the tumor region generated by the pro-posed method. Figure 7 illustrates the areas corresponding to TP, FP, FN, TN, Ω_m, and Ω_a.

In order to further quantitatively evaluate the performance of the proposed fully automatic segmentation scheme, some measures are used in this paper. Figure 8 shows a contingency matrix and measures calculated based on it. Based on the table, it is possible to calculate row and column wise parameters, positive predictive value (PPV, also called precision) and negative predictive value (NPV), sensitivity, and specificity, respectively. PPV and NPV are the conditional probability that a malignant or neutral variant is predicted as malignant or neutral, respectively. Sensitivity is the proportion of breast tumors which have the correct classification in the manual segmentation region. Specificity is the proportion of normal breast tissues which have the correct classification. Accuracy is the proportion of correct segmentation capability in all sub-regions and it is calculated based on all the four figures in the table.

3 Results

In this section, we evaluate the performance of the proposed scheme on a B-mode BUS image dataset of 61 cases, where 32 invasive ductal carcinomas (malignant) and 29 fibroadenomas (benign) have been validated by pathology. The dataset is provided by the Third Affiliated Hospital, Sun Yat-sen University, with various kinds of medical imaging systems, such as ALOKA, PHILIPS, TOSHIBA, HITACHI, and ESAOTE. All images in our dataset contained the breast lesions and pathology reports. The manually delineated tumor boundaries by an experienced radiologist with more than 10 years of experience in reading BUS images (Kai Li, the second author) were used as the golden standards. The proposed fully automatic segmentation algorithm was implemented by using MATLAB (R2013a) on a machine which has a clock speed of 2.94 GHz and 4.0 GB memory with no GPU optimization. The performance of the proposed method was validated by comparing the results with the golden standards.

3.1 Contour initialization results

The aim of the contour initialization scheme is obtaining a reliable lesion region which is located in the inner of the tumor region. Figure 4 shows the segmentation results using the traditional Otsu algorithm and our two-step OBAT pre-segmentation algorithm. Comparing with the results of the traditional Otsu algorithm, the results of the proposed two-step OBAT pre-segmentation method contain fewer false detected areas and will be more easily to find the credible initial contours.

The contour initialization results of our proposed method are shown in Fig. 4. Comparing with the tumor boundaries delineated by the experienced radiologist, it demonstrated that all of the initial contours generated by the proposed method are in the tumor regions.

3.2 Tumor segmentation results

The results of the contour initialization step are used as the initial contours of modified CV model. For brevity, only four representative BUS images (two malignant images and two benign images) from our test database are selected to present the segmentation results as shown in Figs. 9, 10, 11, and 12. The results demonstrate that our automatic initial contour generation scheme is valid for breast lesions with different shapes and sizes and even works well for the breast lesion from the basal and apical sections. Figure 9a shows an irregular malignant tumor, Fig. 10a shows a small malignant tumor, Fig. 11a shows a commonly benign tumor, and Fig. 12a shows a benign tumor which is far away from the center of the image. Figures 9b, 10b, 11b, and 12b show the filtered images, in which most of the speckles have been removed by NLLR model. Figures 9c, 10c, 11c, and 12c show the pre-segmentation results using the proposed automatic threshold presegmentation algorithm. Figures 9d, 10d, 11d, and 12d show the initial contour generated by the proposed automatic initial contour generation method. Figures 9e, 10e, 11e, and 12e show the initial contours of the original image. Figures 9f, 10f, 11f, and 12f show the final contours delineated by the green lines. From the results of our proposed method, it can be clearly observed that the contours produced by our approach are located in the true contour of the tumor area wherever the true tumor located in the BUS image.

To demonstrate the advantages of the proposed CV-ROEWA model, it is compared with the standard CV model using the same initial contour which is generated by the contour initialization scheme. We follow the algorithm in [24] exactly and test it on the same database. The results after a series of operations with pre-processing, contour initialization, and CV model are shown in Fig. 13. The upper row of Fig. 13 shows the results of the standard CV model with 100 iterations, 300 iterations, 500 iterations, and 1000 iterations. The lower row of Fig. 13 shows the results of our CV-ROEWA model with 100 iterations, 300 iterations, 500 iterations, and 1000 iterations. It is obviously seen that the final contour produced by the CV model may easy cross the true contour with the increase of iterations. And the curve evolution using the CV-ROEWA model will stop when the curve evolves the real boundary contour of the tumor.

In order to validate the effectiveness of the proposed scheme, we compared the proposed method with the currently published method in [34]. We follow the algorithm in [34] exactly and test it on our datasets. For all of the 61 BUS images in our database, Elawady's method totally fails to segment the lesion in 11 images; this is because the output result of their segmentation tool is not correctly segmented; as a result, the post-processing step is just neglecting any region rather than the lesion. One typical case with incorrect segmentation using Elawady's method is shown in Fig. 14d. The proposed scheme is effective in all the test images.

The segmentation results of the proposed scheme and Elawady's in four BUS images are shown in Fig. 14. Figure 14a–d shows the results of Elawady's method, Fig. 14e–h shows the results using the contour initialization + standard CV model, Fig. 14 i–l shows the results of the contour initialization + CV-ROEWA model, and Fig. 14 m–p shows the results of manual segmentation by the radiologist. It is obviously seen that the contours produced by

the contour initialization + CV-ROEWA model are closer to the true contour of the tumor area.

The quantitative analysis of the segmentation results of Elawady's method, initial contour + CV, and initial contour + CV-ROEWA in the dataset images is listed in Tables 1, 2, 3, and 4, where the values include the mean and standard deviations results. Table 1 and Table 2 show the area error metrics of benign and malignant images, respectively. The segmentation accuracy, sensitivity, specificity, PPV, and NPV are illustrated in Table 3 and Table 4, respectively.

The Kruskal-Wallis method is used to test the significance of the differences among the three methods. The p values obtained are shown in Table 5. To further reveal if there are statistical differences between each pair of Elawady's method, the initial contour + CV model, and the initial contour + CV-ROEWA model, the post hoc analysis is performed which is based on Tukey-Kramer method and a 95% confidence inter-val. The result of post hoc analysis is shown in Table 6.

3.3 Classification of breast cancer using morphological features

Morphological features have been proved to be effective features in differentiating benign from malignant breast tumors with high accuracy [31]. Circularity, elongation, compactness, orientation, and radial distance standard deviation are the most common and most effective morphological features for evaluating benign or malignant of breast tumors in clinical application [31–33]. The five morphologic features formed the input to a support vector machine (SVM) to distinguish the benign tumors from malignant ones. In the experiments, we use 41 cases (including 19 benign breast tumors and 22 malignant ones) to train the SVM and the remaining 20 cases (including 10 benign breast tumors and 10 malignant ones) to test the SVM. The morphological features of circularity, elongation, compactness, orientation, and radial distance standard deviation are extracted from the results of CV model, manual segmentation, and the proposed method. The experimental result is listed in Table 7 and the ROC analysis is shown in Fig. 15.

4 Discussion

Initial contour generation is a prerequisite step for this automatic segmentation scheme of BUS images. The initial contour provided by the proposed contour initialization method can provide a rough location of the lesion. In the case of low contrast, it is difficult to exclude normal tissues and artifacts via the traditional Otsu method. To address this problem, we propose an adaptive thresholding method for low contrast images. In our method, the contour initialization outputs are close to the true boundaries of the tumor. Hence, fewer iterations are required in the subsequent processing.

Tables 1, 2, 3 and 4 list the quantitative analysis results of these three methods. The TP of the proposed method is larger than Elawady's method and CV model, indicating that the segmented area of our method covers more area of the true tumor. The FP and FN of the proposed method are better than Elawady's method. For the metric JS, the proposed method is closer to 1 than Elawady's method and CV model, proving that the contours detected by

our method are more similar to the manual segmentation. From Table 3 and Table 4, it can be clearly observed that the accuracy, sensitivity, specificity, PPV, and NPVof our proposed method are larger than Elawady's method and initial contour + CV model, further proving that the contours detected by our method are more effective and more accurate in the studied database. The results show that the proposed model achieves better overall performance than both the CV model and Elawady's method.

The p values obtained by Kruskal-Wallis test are shown in Table 5. It can be seen that the difference among the three methods is significant. The result of post hoc analysis is reported in Table 6. It can be seen that the p_{12} values of accuracy, sensitivity, specificity, PPV, and NPV are all less than 0.05, indicating there is a significant difference between Elawady's method and initial contour + CV model. All the p_{13} values of accuracy, sensitivity, specificity, PPV, and NPV are much smaller, indicating the significant difference between the results of Elawady's method and initial contour + CV-ROEWA model. All the p_{23} values are not less than 0.05, indicating there is no significant difference between the initial contour + CV model and the initial contour + CV-ROEWA model. However, we believe no significance does not mean unimportance. As mentioned in section 3.2, CV-ROEWA model shows better convergence than CV model with the increase of iterations.

Moreover, with the recent development of radiomics and radiogenomics in breast cancer [35–39], we expect this proposed method would facilitate such analysis of BUS images and generate interesting findings. The limit of the proposed scheme is that the largest region criterion in contour initialization could reduce the efficiency of the method in cases with multiple tumors, because the detection of a second mass is deliberately ignored.

5 Conclusions

In this paper, we propose an automatic segmentation framework for breast ultrasound image. The approach based on semiautomatic or manual segmentation is time-consuming and difficult to reproduce. In addition, some popular semiautomatic segmentation methods rely on the initial contour. Hence, this paper proposes an automatic contour initialization scheme to automatically obtain the initial contour. And a new CV-ROEWA mod-el is proposed to further refine the contours of the tumor regions. Qualitative and quantitative analyses in clinical BUS images illustrate the proposed method is superior to previous segmentation models in terms of accuracy and robustness.

In future work, we plan to test the proposed model with more clinical data and further expand our model for classification of the benign or malignant tumors.

Acknowledgments

Funding information This work is partially supported by grants from the National Natural Science Foundation of China (NSFC: 61401451, 61501444, 61472411), Guangdong Province Science and Technology Plan Projects (Grant No. 2015B020233004), and Shenzhen Technology Research Project (Grant No. JSGG20160429192140681, JCYJ20160429174611494).

Biographies

Lei Liu is currently a research assistant in Shenzhen Institutes of Advanced Technology, Chinese Academy of Sciences. Her current research interests focus on medical imaging processing and analysis.

Kai Li is currently a radiologist at the Third Affiliated Hospital of Sun Yat-Sen University. His scientific interests include ultrasound-guided tumor ablation treatment, ultrasound involved in image fusion, and tumor thermal ablation treatment planning based on computer image processing.

Wenjian Qin is currently a PhD candidate in Pattern Recognition and Intelligent System at the University of Chinese Academy of Sciences since 2015 and also joins a visiting PhD student program at Radiology Oncology Department, Stanford University. He joined the Shenzhen Institutes of Advanced Technology, Chinese Academy of Sciences, as an Assistant Professor since June 2012. His research interest is medical image analysis using machine learning.

Dr. Tiexiang Wen is currently an associate professor in Shenzhen Institutes of Advanced Technology, Chinese Academy of Sciences. His current research interests focus on medical imaging processing and image-guided interventions.

Dr. Ling Li is currently a senior engineer in Shenzhen Institutes of Advanced Technology, Chinese Academy of Sciences. Her current research interests focus on stereo vision-guided treatment.

Dr. Jia Wu is a postdoctoral researcher at the Department of Radiation Oncology of Stanford University. His research focuses on medical image analysis, image genomic analysis, and their applications in oncology settings. He received his PhD degree from the University of Pittsburgh in 2013.

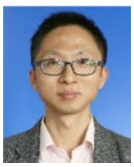

Dr. Jia Gu (IEEE Senior Member) is currently a Professor in Shenzhen Institutes of Advanced Technology of Chinese Academy of Sciences. He received his master and PhD degree in 2001 and 2005 from Southeast University (China) and University of Rennes (France), respectively. His research focuses on computer vision and medical imaging.

References

1. Mustra M, Grgic M, Rangayyan RM (2016) Review of recent advances in segmentation of the breast boundary and the pectoral muscle in mammograms. Med Biol Eng Comput 54(7):1003–1024. 10.1007/s11517-015-1411-7 [PubMed: 26546074]
2. Anitha J, Peter JD (2015) Mammogram segmentation using maximal cell strength updation in cellular automata. Med Biol Eng Comput 53(8):737–749. 10.1007/s11517-015-1280-0 [PubMed: 25841356]
3. Chang RF, WJ W, WK Moon, Chen DR (2005) Automatic ultra-sound segmentation and morphology based diagnosis of solid breast tumors. Breast Cancer Res Treat 89(2):179–185. 10.1007/s10549-004-2043-z [PubMed: 15692761]
4. Drukker K, Giger ML, Horsch K, Kupinski MA, Vyborny CJ, Mendelson EB (2002) Computerized lesion detection on breast ultrasound. Med Phys 29(7):1438–1446. 10.1118/1.1485995 [PubMed: 12148724]
5. Joo S, Yang YS, Moon WK, Kim HC (2004) Computer-aided diagnosis of solid breast nodules: use of an artificial neural network based on multiple sonographic features. IEEE Trans Med Imaging 23(10):1292–1300. 10.1109/TMI.2004.834617 [PubMed: 15493696]
6. Horsch K, Giger ML, Venta LA, Vyborny CJ (2002) Computerized diagnosis of breast lesions on ultrasound. Med Phys 29(2):157–164. 10.1118/1.1429239 [PubMed: 11865987]

7. Huang YL, Chen DR (2004) Watershed segmentation for breast tumor in 2-D sonography. Ultrasound Med Biol 30(5):625–632. 10.1016/j.ultrasmedbio.2003.12.001 [PubMed: 15183228]
8. Gomez W, Leija L, Alvarenga AV, Infantosi AFC, Pereira WCA (2010) Computerized lesion segmentation of breast ultrasound based on marker-controlled watershed transformation. Med Phys 37(1):82–95. 10.1118/1.3265959 [PubMed: 20175469]
9. Boukerroui D, Basset O, Guerin N, Baskurt A (1998) Multiresolution texture based adaptive clustering algorithm for breast lesion segmentation. Eur J Ultrasound 8(2):135–144. 10.1016/S0929-8266(98)00062-7 [PubMed: 9845797]
10. Huang QH, Lee SY, Liu LZ, MH L, Jin LW, Li AH (2012) A robust graph-based segmentation method for breast tumors in ultrasound images. Ultrasonics 52(2):266–275. 10.1016/j.ultras.2011.08.011 [PubMed: 21925692]
11. Huang YL, Jiang YR, Chen DR, Moon WK (2007) Level set contouring for breast tumor in sonography. J Digit Imaging 20(3): 238–247. 10.1007/s10278-006-1041-6 [PubMed: 17252171]
12. Li C, Xu C, Gui C, Fox MD (2010) Distance regularized level set evolution and its application to image segmentation. IEEE Trans Image Process 19(12):3243–3254. 10.1109/TIP.2010.2069690 [PubMed: 20801742]
13. Madabhushi A, Metaxas DN (2003) Combining low-, high-level and empirical domain knowledge for automated segmentation of ultrasonic breast lesions. IEEE Trans Med Imaging 22(2):155–169 10.1109/TMI.2002.808364 [PubMed: 12715992]
14. Liu X, Huo Z, Zhang J (2006) Automated segmentation of breast lesions in ultrasound images. In: 27th Annual International Conference of the IEEE-EMBS, pp 7433–7435
15. Shan J, Cheng HD, Wang Y (2012) Completely automated segmentation approach for breast ultrasound images using multiple-domain features. Ultrasound Med Biol 38(2):262–275. 10.1016/j.ultrasmedbio.2011.10.022 [PubMed: 22230134]
16. Xian M, Zhang Y, Cheng HD (2015) Fully automatic segmentation of breast ultrasound images based on breast characteristics in space and frequency domains. Pattern Recogn 48(2):485–497. 10.1016/j.patcog.2014.07.026
17. Zhu L, Fu CW, Brown MS, Heng PA (2017) A non-local low-rank framework for ultrasound speckle reduction. In: 2017 I.E. Computer Society Conference on Computer Vision and Pattern Recognition (CVPR'17), PP 5650–5658
18. Yu Y, Acton ST (2002) Speckle reducing anisotropic diffusion. IEEE Trans Image Process 11(11): 1260–1270. 10.1109/TIP.2002.804276 [PubMed: 18249696]
19. Cardoso FM, Matsumoto MM, Furuie SS (2012) Edge-preserving speckle texture removal by interference-based speckle filtering followed by anisotropic diffusion. Ultrasound Med Biol 38(8): 1414–1428. 10.1016/j.ultrasmedbio.2012.03.014 [PubMed: 22698511]
20. Flores WG, Pereira WCA, Infantosi AFC (2014) Breast ultrasound despeckling using anisotropic diffusion guided by texture descrip-tors. Ultrasound Med Biol 40(11):2609–2621. 10.1016/j.ultrasmedbio.2014.06.005 [PubMed: 25218452]
21. Zhu L, Wang W, Qin J, Wong KH, Choi KS, Heng PA (2017) Fast feature-preserving speckle reduction for ultrasound images via phase congruency. Signal Process 134:275–284. 10.1016/j.sigpro.2016.12.011
22. Mittal D, Kumar V, Saxena SC, Khandelwal N, Kalra N (2010) Enhancement of the ultrasound images by modified anisotropic diffusion method. Med Biol Eng Comput 48(12):1281–1291. 10.1007/s11517-010-0650-x [PubMed: 20574722]
23. Otsu N (1979) A threshold selection method from gray-level histo-grams. IEEE Trans Syst Man Cybern 9(1):62–66. 10.1109/TSMC.1979.4310076
24. Chan TF, Vese LA (2001) Active contours without edges. IEEE Trans Image Process 10(2):266–277. 10.1109/83.902291 [PubMed: 18249617]
25. Loizou CP, Pattichis CS, Pantziaris M, Tyllis T, Nicolaides A (2007) Snakes based segmentation of the common carotid artery intima media. Med Biol Eng Comput 45(1):35–49. 10.1007/s11517-006-0140-3 [PubMed: 17203319]
26. Mumford D, Shah J (1989) Optimal approximations by piecewise smooth functions and associated variational problems. Commun Pure Appl Math 42(5):577–685. 10.1002/cpa.3160420503

27. Li C, Xu C, Gui C, Fox MD (2005) Level set evolution without re-initialization: a new variational formulation. In: 2005 I.E. Computer Society Conference on Computer Vision and Pattern Recognition (CVPR'05), pp 430–436
28. Fjortoft R, Lopes A, Marthon P, Cubero-Castan E (1998) An optimal multiedge detector for SAR image segmentation. IEEE Trans Geosci Remote Sens 36(3):793–802. 10.1109/36.673672
29. Rodrigues R, Braz R, Pereira M, Moutinho J, Pinheiro AM (2015) A two-step segmentation method for breast ultrasound masses based on multi-resolution analysis. Ultrasound Med Biol 41(6): 1737–1748. 10.1016/j.ultrasmedbio.2015.01.012 [PubMed: 25736608]
30. Xu X, Niemeijer M, Song Q, Sonka M, Garvin MK, Reinhardt JM, Abràmoff MD (2011) Vessel boundary delineation on fundus images using graph-based approach. IEEE Trans Med Imaging 30(6): 1184–1191. 10.1109/TMI.2010.2103566 [PubMed: 21216707]
31. Huang YL, Chen DR, Jiang YR, Kuo SJ, Wu HK, Moon WK (2008) Computer-aided diagnosis using morphological features for classifying breast lesions on ultrasound. Ultrasound Obstet Gynecol 32(4):565–572. 10.1002/uog.5205 [PubMed: 18383556]
32. Wu WJ, Moon WK (2008) Ultrasound breast tumor image computer-aided diagnosis with texture and morphological features. Acad Radiol 15(7):873–880 [PubMed: 18572123]
33. Moon WK, Chen IL, Chang JM, Shin SU, Lo CM, Chang RF (2017) The adaptive computer-aided diagnosis system based on tumor sizes for the classification of breast tumors detected at screening ultrasound. Ultrasonics 76:70–77. 10.1016/j.ultras.2016.12.017 [PubMed: 28086107]
34. Elawady M, Sadek I, Shabayek AER, Pons G, Ganau S (2016) Automatic nonlinear filtering and segmentation for breast ultra-sound images. In: International conference image analysis and recognition Springer International Publishing, Switzerland, pp 206–213. 10.1007/978-3-319-41501-7_24
35. Wu J, Li B, Sun X, Cao G, Rubin DL, Napel S, Ikeda DM, Kurian AW, Li R (2017) Heterogeneous enhancement patterns of tumor-adjacent parenchyma at MR imaging are associated with dysregulated signaling pathways and poor survival in breast cancer. Radiology 285(2):401–413. 10.1148/radiol.2017162823 [PubMed: 28708462]
36. Wu J, Cui Y, Sun X, Cao G, Li B, Ikeda DM, Kurian AW, Li R (2017) Unsupervised clustering of quantitative image phenotypes reveals breast cancer subtypes with distinct prognoses and molecular pathways. Clin Cancer Res 10.1158/1078-0432.CCR-16-2415
37. Wu J, Sun X, Wang J, Cui Y, Kato F, Shirato H, Ikeda DM, Li R (2017) Identifying relations between imaging phenotypes and molecular subtypes of breast cancer: model discovery and external validation. J Magn Reson Imaging 10.1002/jmri.25661
38. Wu J, Gong G, Cui Y, Li R (2016) Intratumor partitioning and texture analysis of dynamic contrast-enhanced (DCE)-MRI identifies relevant tumor subregions to predict pathological response of breast cancer to neoadjuvant chemotherapy. J Magn Reson Imaging 44(5):1107–1115. 10.1002/jmri.25279 [PubMed: 27080586]
39. Ertas G, Doran SJ, Leach MO (2017) A computerized volumetric segmentation method applicable to multicentre MRI data to support computer-aided breast tissue analysis, density assessment and lesion localization. Med Biol Eng Comput 55(1):57–68. 10.1007/s11517-016-1484-y [PubMed: 27106750]

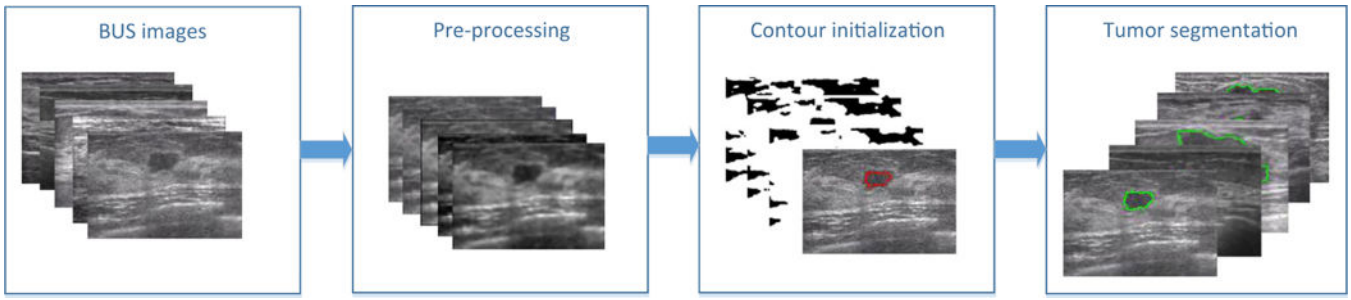

Fig. 1.
The main framework of the proposed scheme for BUS images segmentation

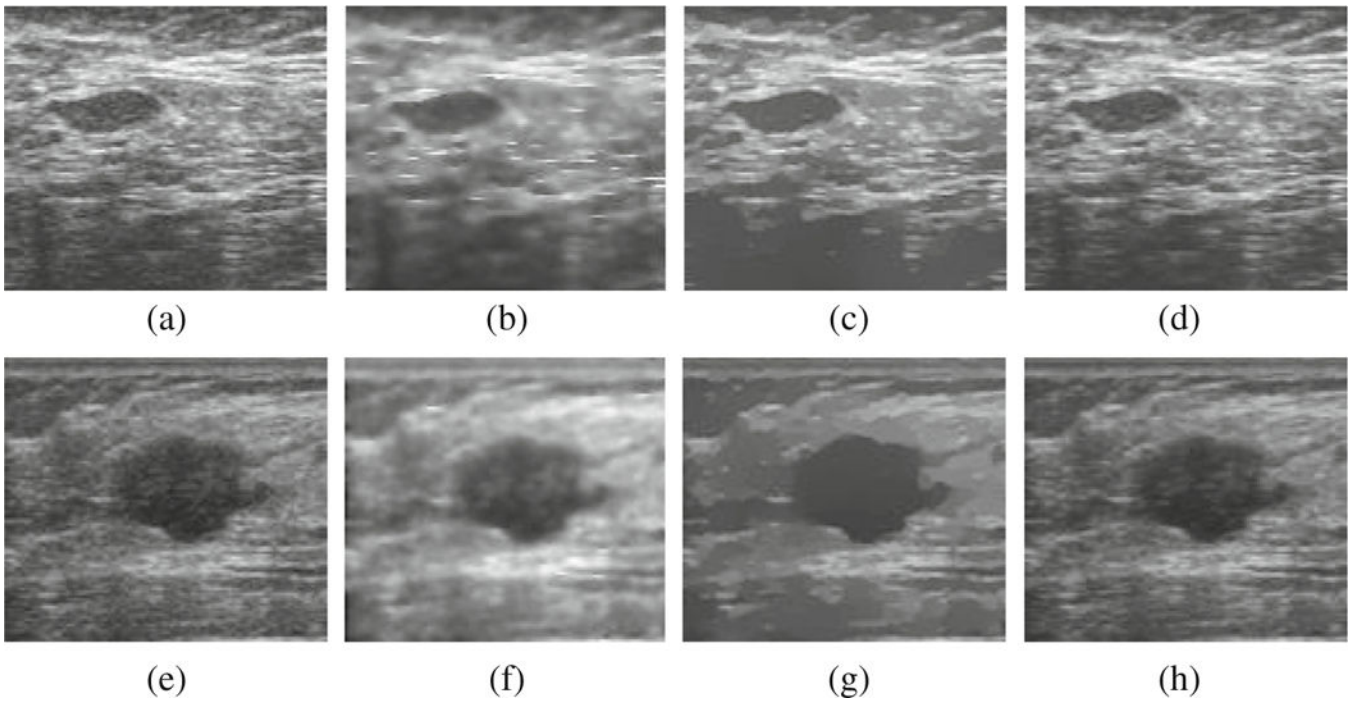

Fig. 2.

Comparisons of speckle reduction using different filtering schemes. **a**, **e** Original images. **b**, **f** The filtered images using the SRAD model. **c**, **g** The filtered images using SRPC model. **d, h** The filtered images using the NLLR model

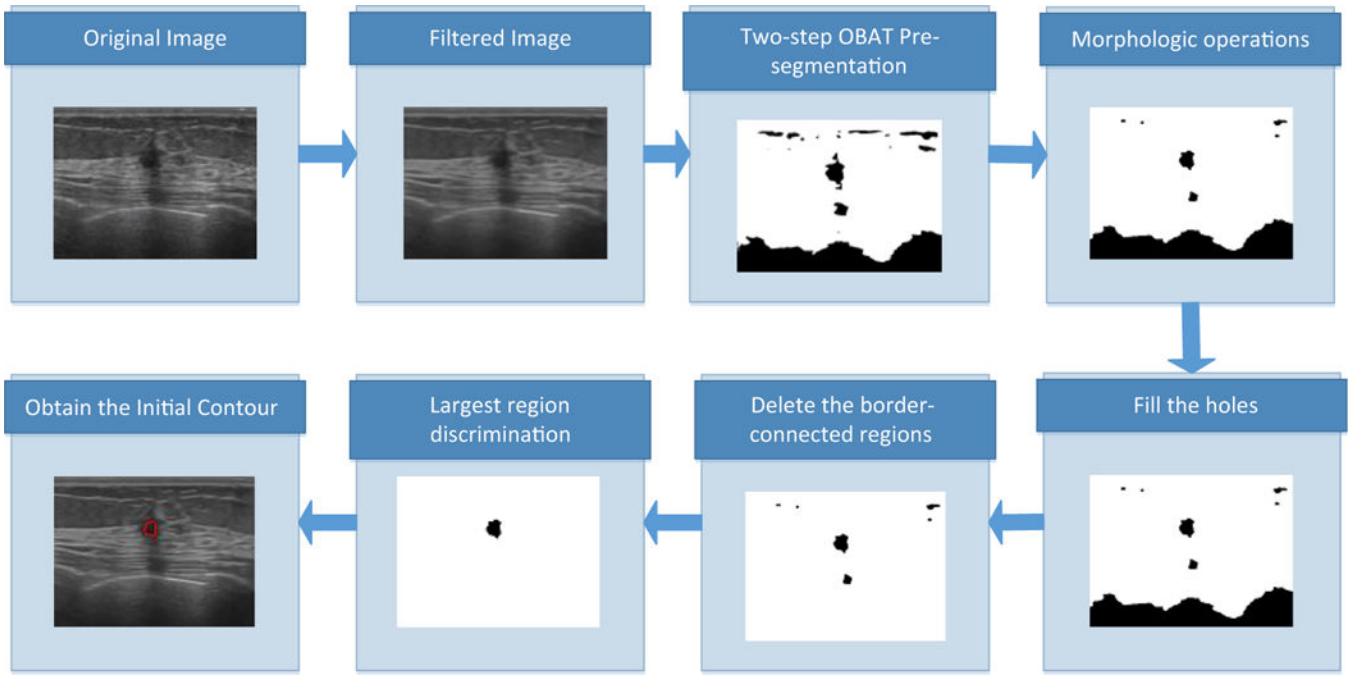

Fig. 3.
Flow chart of the contour initialization scheme

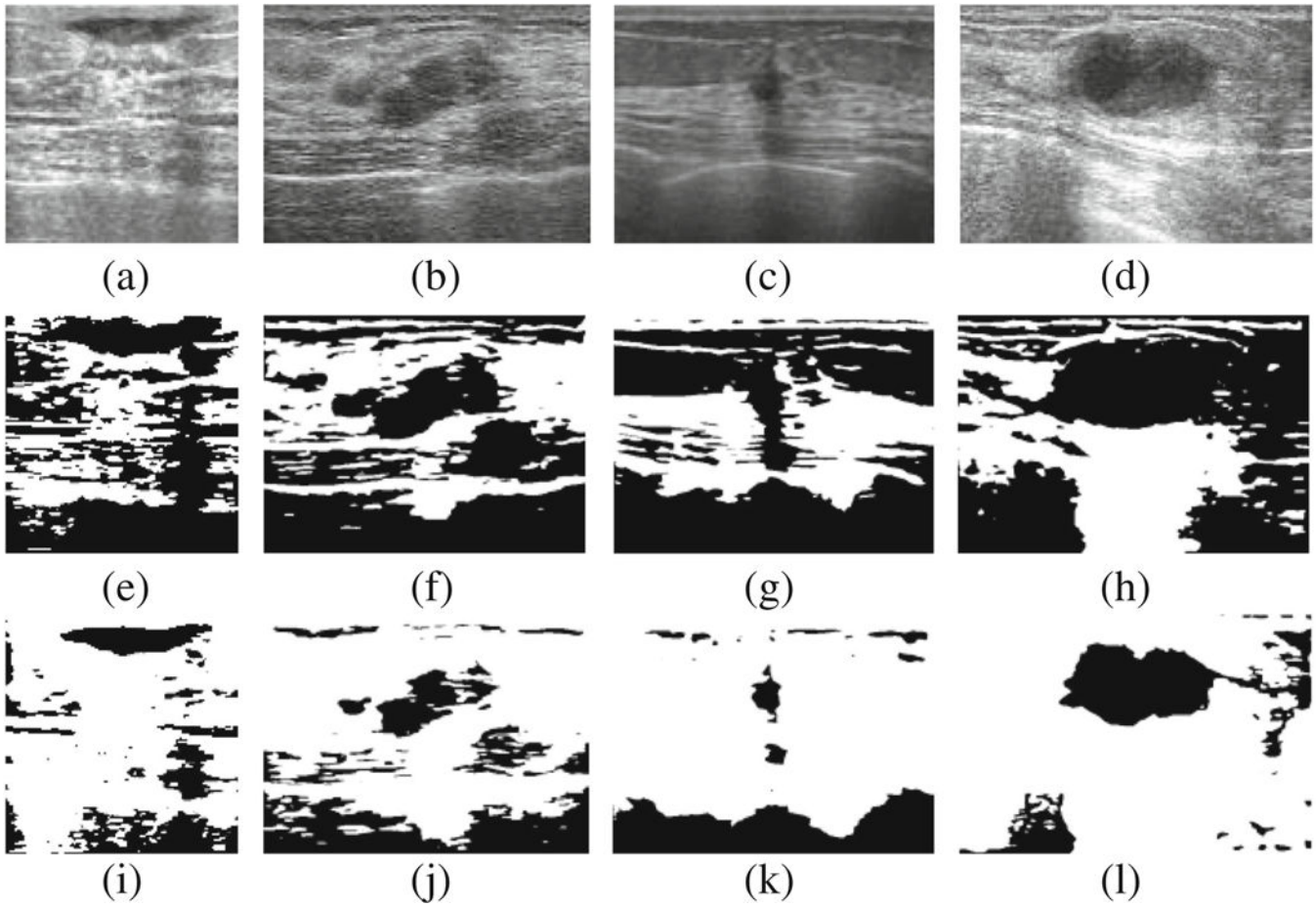

Fig. 4.

A comparison between the Otsu method and the proposed modified Otsu threshold selection method. **a–d** Original images. **e–h** Binary images generated using Otsu method. **i–l** Binary images generated using the modified Otsu method

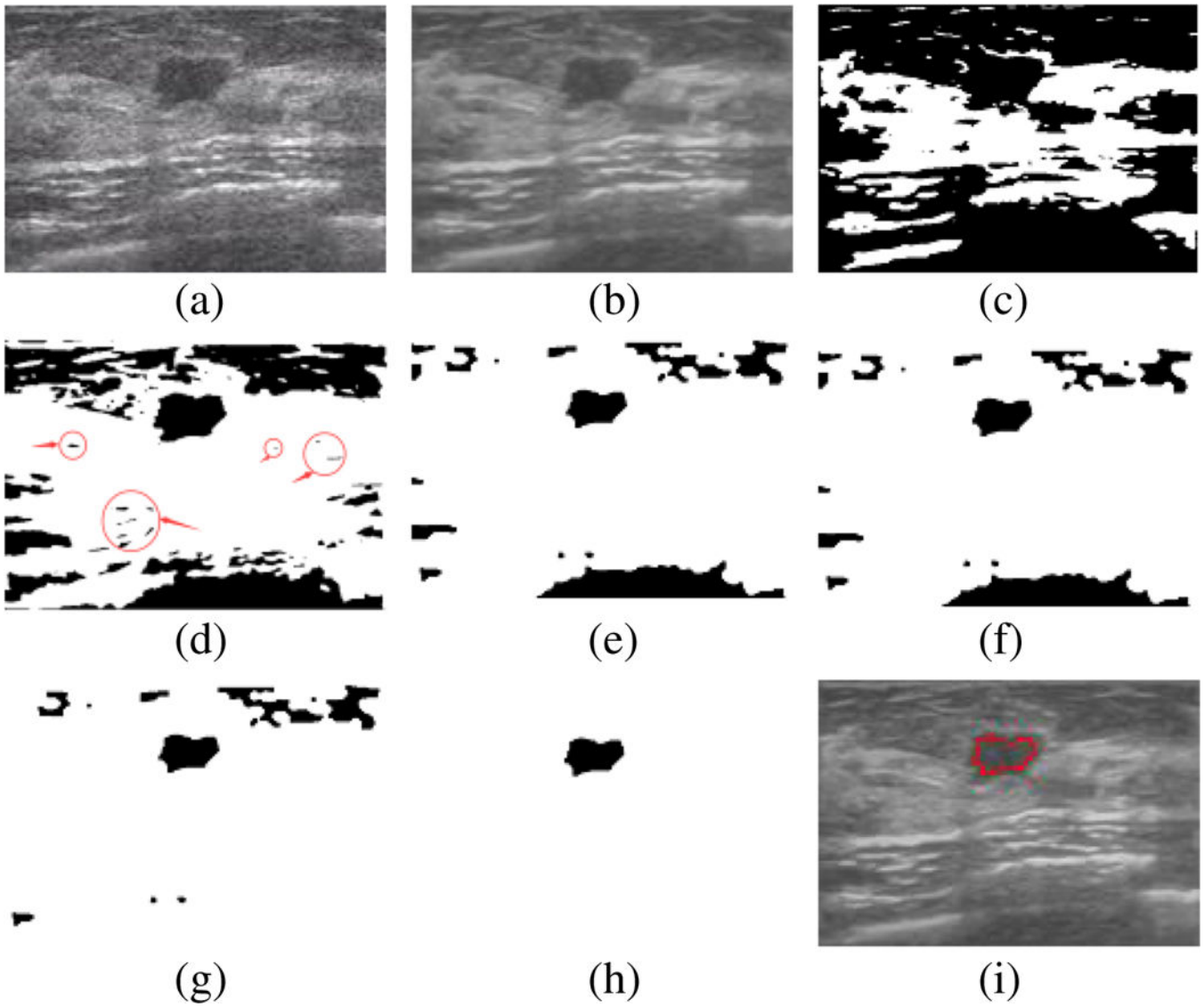

Fig. 5.

The process of initial contour generation. **a** Original image. **b** Filtered image. **c** Result of traditional Otsu method. **d** Result of the proposed adaptive thresholding method. **e** Result of morphologic operations. **f** Result of filling the holes. **g** Result of deleting border-connected regions. **h** Result of the largest region discrimination. **i** The initial contour overlapping the original image. (The red circles indicate the small isolated misclassified regions)

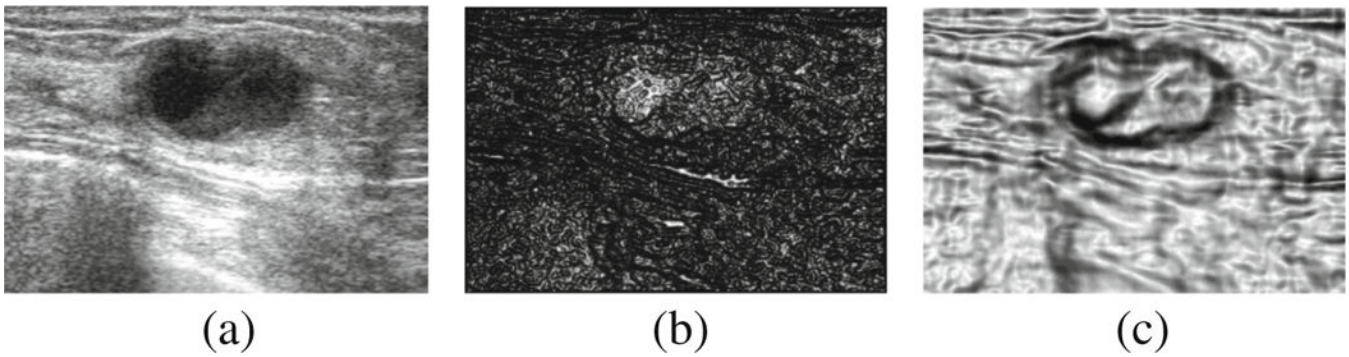

Fig. 6.

A comparison between the gradient-based edge detectors and the ROEWA-based edge detectors. **a** The original image. **b** The gradient-based edge detectors. **c** The ROEWA-based edge detectors

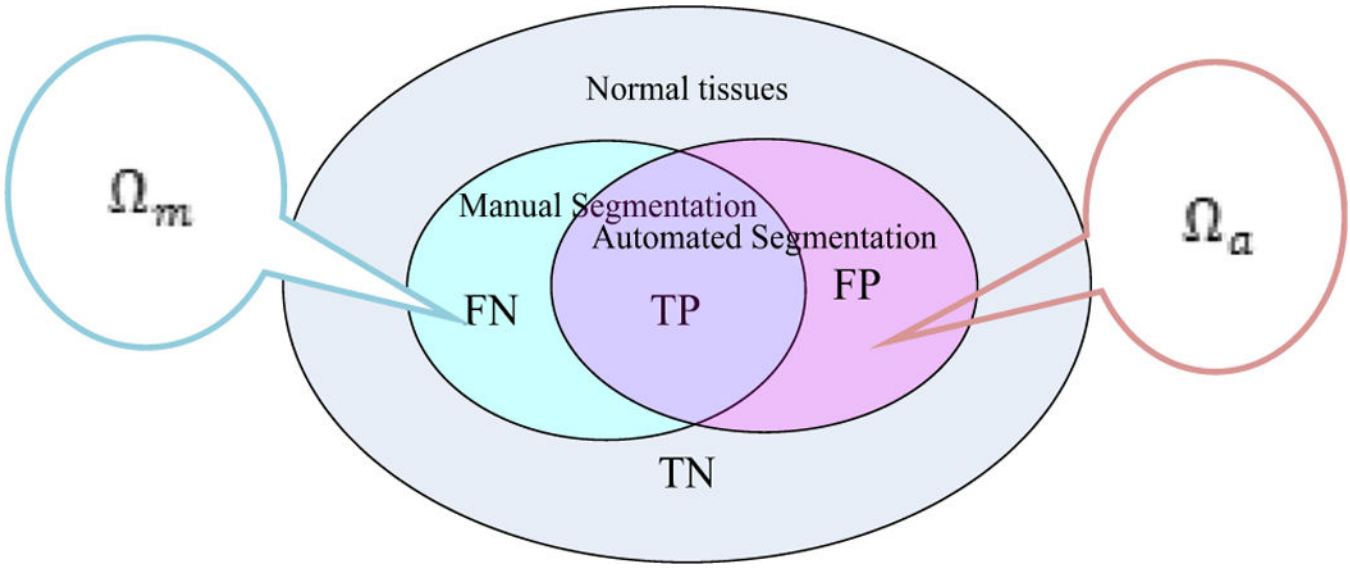

Fig. 7.
Illustration of the areas corresponding to TP, FP, FN, TN, Ω_m, and Ω_a

True Positive (TP)	False Positive (FP)	Positive Predictive value (PPV) $\frac{TP}{TP+FP}$
False Negative (FN)	True Negative (TN)	Negative Predictive value (NPV) $\frac{TN}{FN+TN}$
Sensitivity $\frac{TP}{TP+FN}$	Specificity $\frac{TN}{FP+TN}$	Accuracy $\frac{TP+TN}{TP+FP+FN+TN}$

Fig. 8.
Contingency matrix of measures

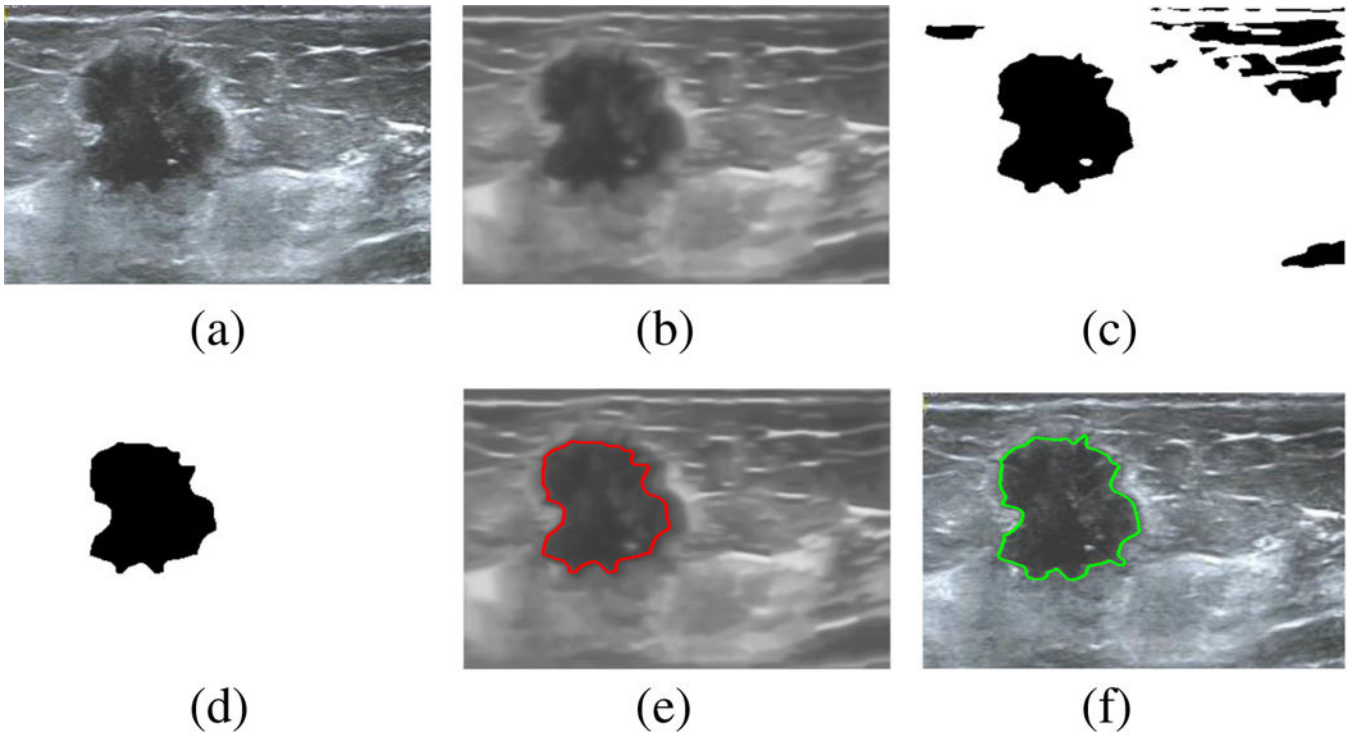

Fig. 9.

Segmentation results for the first malignant BUS image: **(a)** original image; **(b)** filtered image; **(c)** result of the automatic threshold pre-segmentation; **(d)** the initial contour; **(e)** the initial contour of the original image; **(f)** the final result.

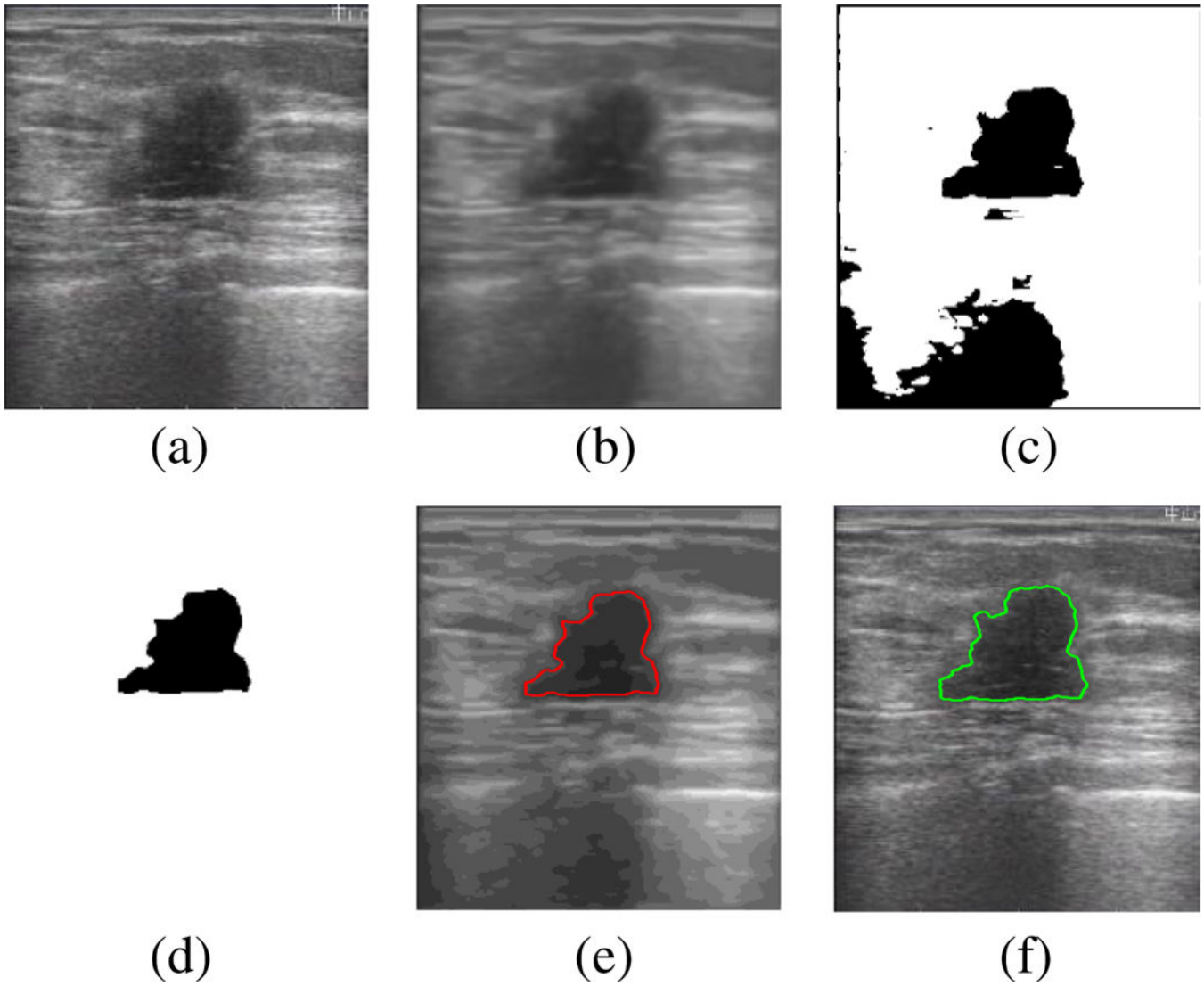

Fig. 10.

Segmentation results for the second malignant BUS image. **a** Original image. **b** Filtered image. **c** The result of the automatic threshold pre-segmentation. **d** The initial contour. **e** The initial contour of the original image. **f** The final result

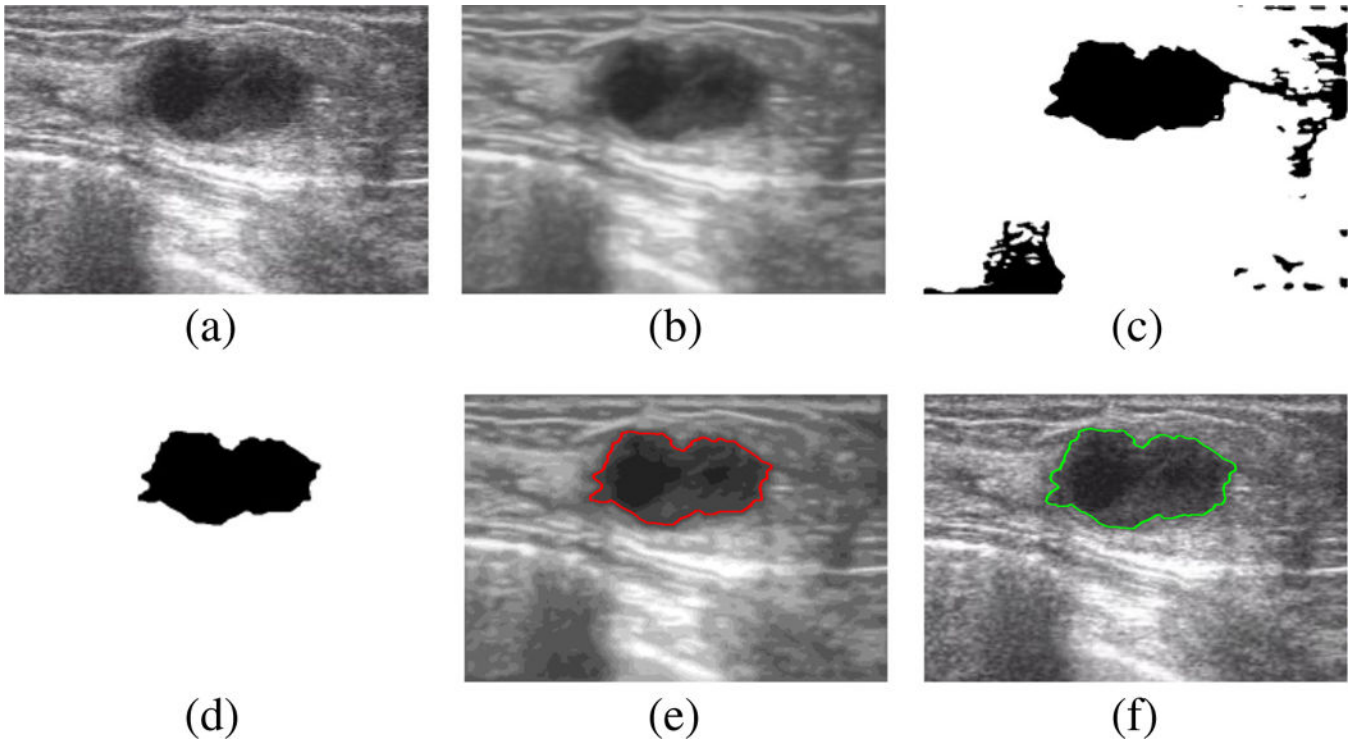

Fig. 11.

Segmentation results for the first benign BUS image. **a** Original image. **b** Filtered image. **c** The result of automatic threshold pre-segmentation. **d** The initial contour. **e** The initial contour of the original image. **f** The final result

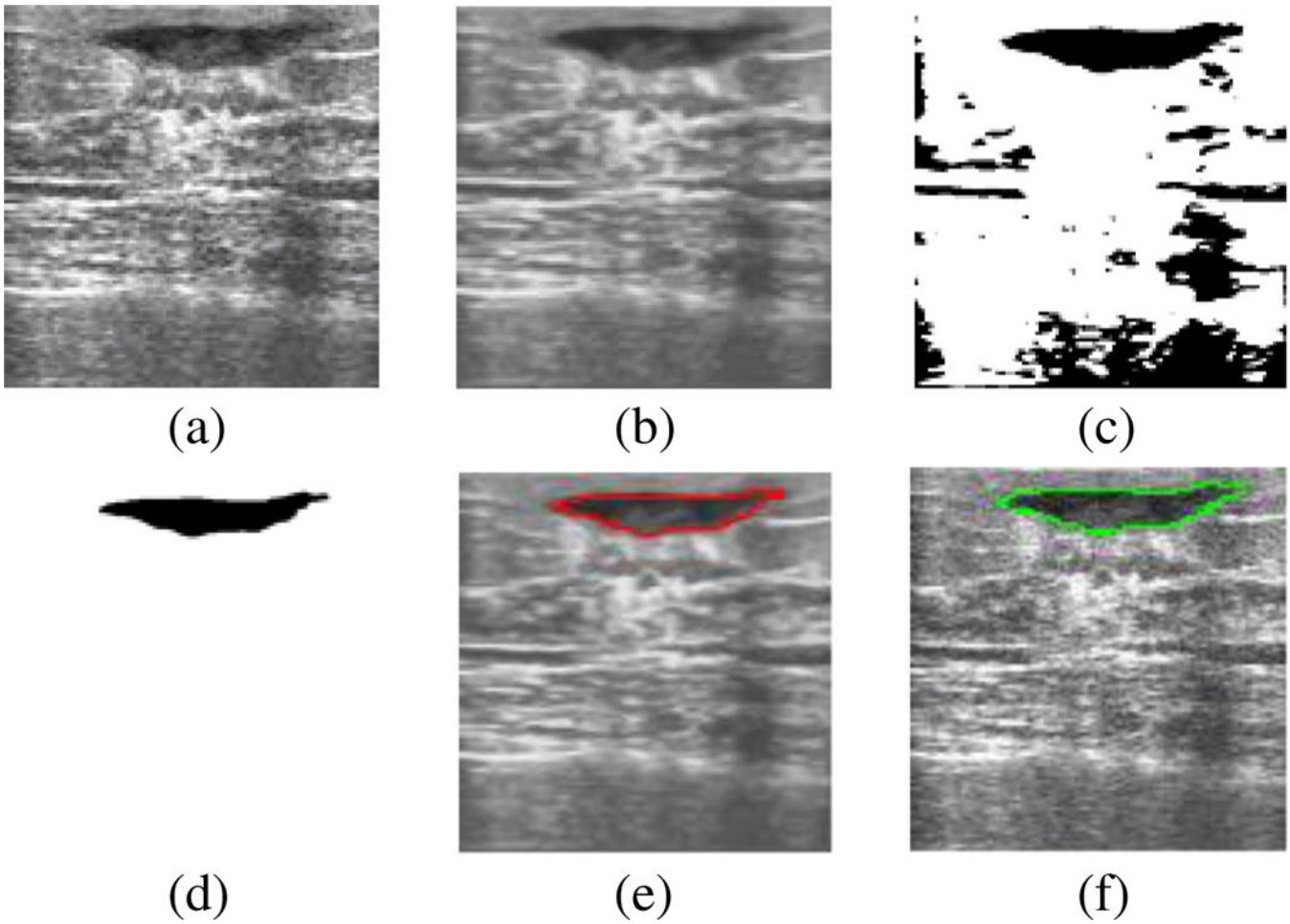

Fig. 12.

Segmentation results for the second benign BUS image. **a** Original image. **b** Filtered image. **c** The result of automatic threshold pre-segmentation. **d** The initial contour. **e** The initial contour of the original image. **f** The final result

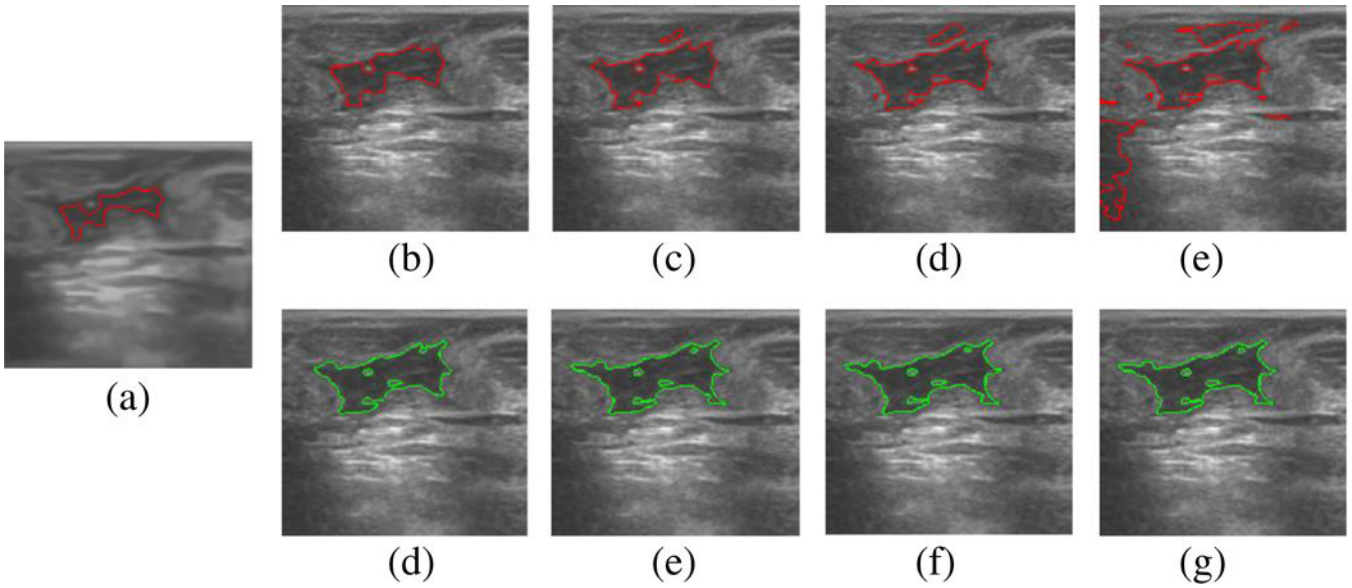

Fig. 13.

A comparison between the CV model and the CV-ROEWA model. **a** The original imag., **b–**e The results using the CV model. **f–**i The results using the CV-ROEWA mode. **b, f** 100 iterations. **c**, **g** 300 iterations. **d**, **h** 500 iterations. **e**, i 1000 iterations

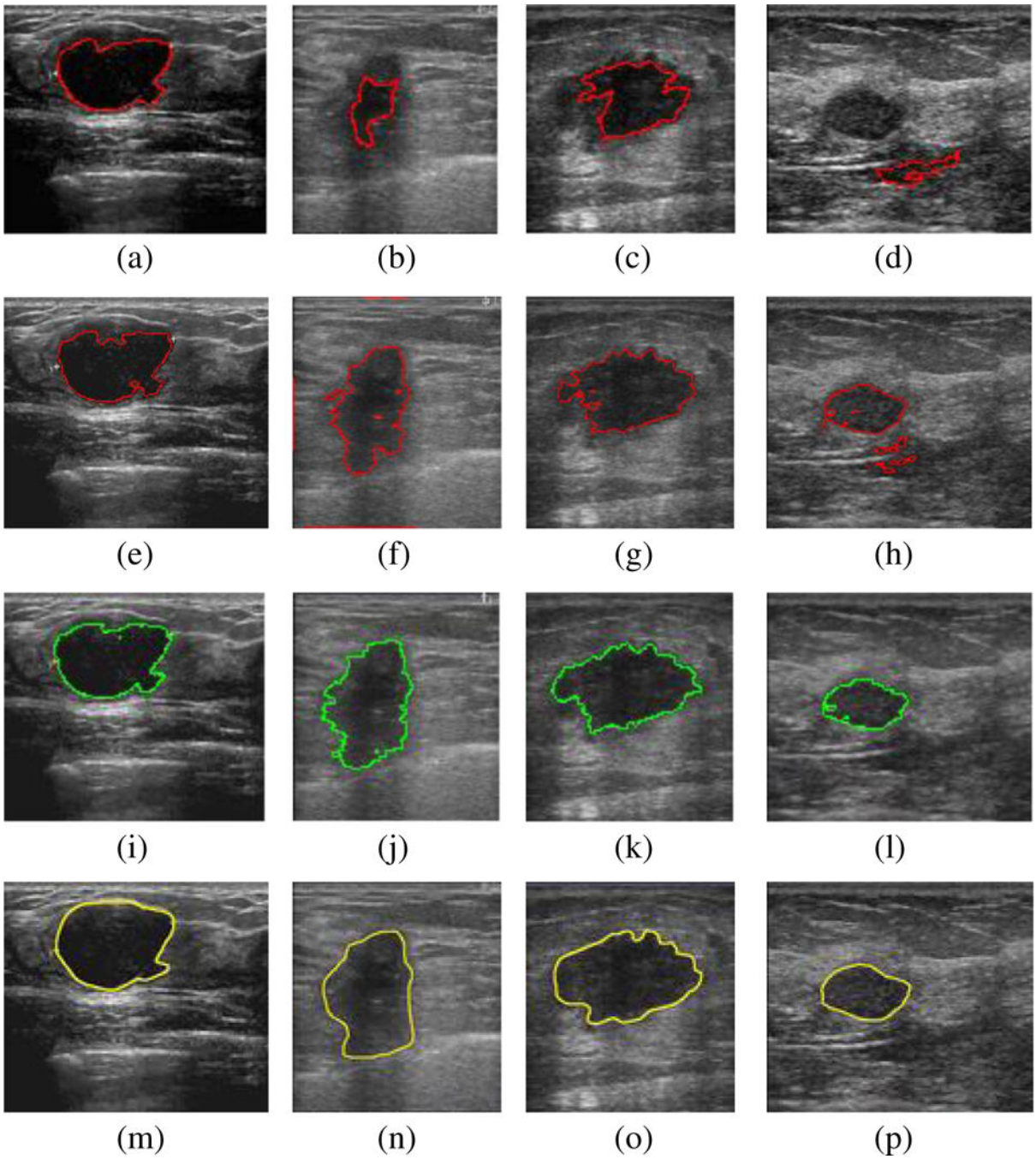

Fig. 14.

Comparison of breast tumor segmentation in clinical ultrasound images. **a–d** The segmentation results using Elawady's method. **e–h** The segmentation results using the contour initialization + standard CV model. i–l The segmentation results produced by the contour initialization + CV-ROEWA model. **m–p** The manual segmentation results by the radiologist

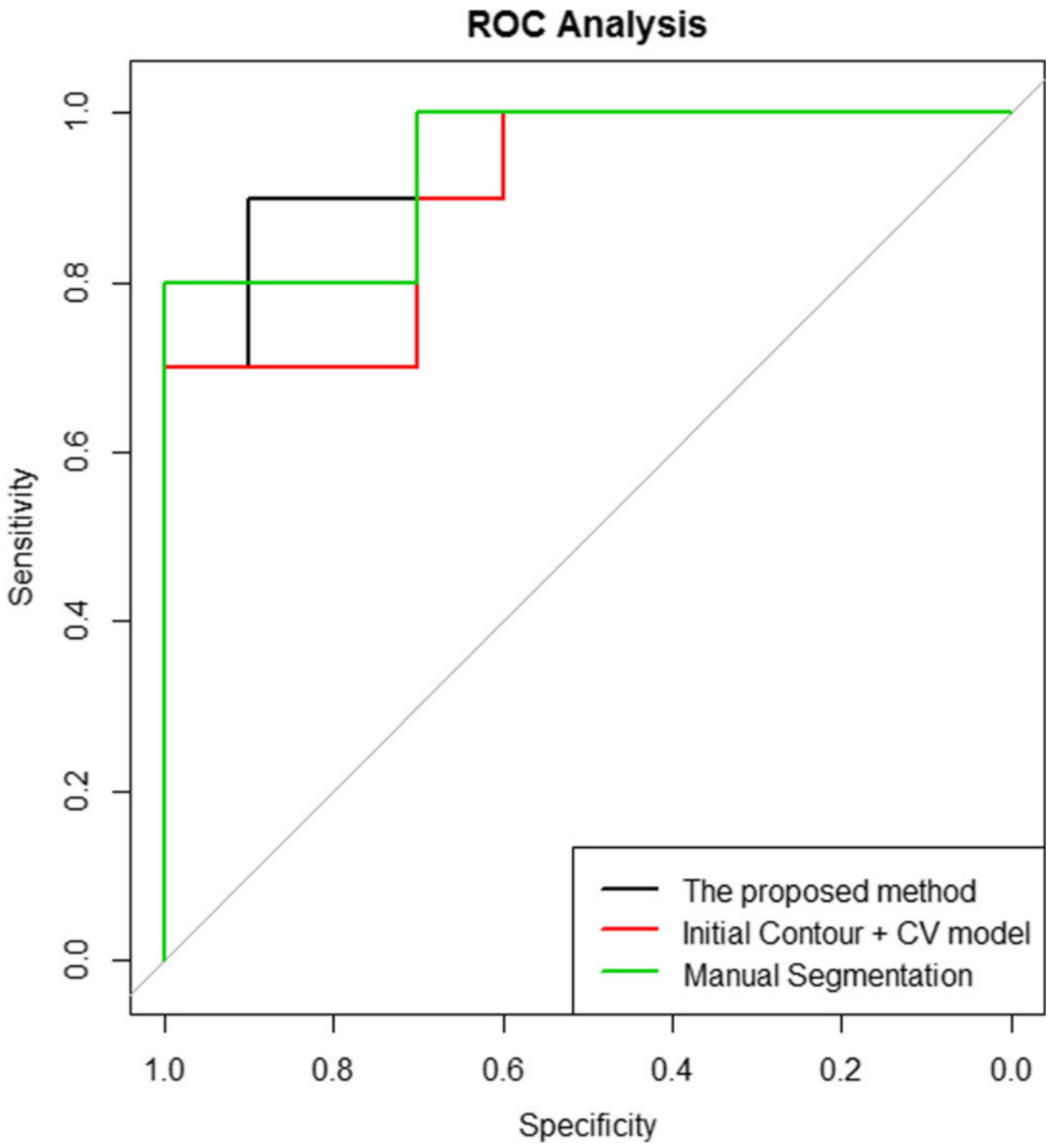

Fig. 15.
ROC curves of classification

Table 1

Statistical evaluation with area error metrics of benign tumors

Methods	TP (%)	FP (%)	FN (%)	JS (%)
Elawady's method	70.39 ± 18.57	1.62 ± 2.40	29.61 ± 18.57	68.52 ± 17.65
Initial contour + CV	84.92 ± 5.59	8.51 ± 15.15	15.08 ± 5.59	78.10 ± 11.67
Initial contour +CV-ROEWA	87.84 ± 5.43	2.42 ± 2.05	12.16 ± 5.43	85.29 ± 5.20

Table 2

Statistical evaluation with area error metrics of malignant tumors

Methods	TP (%)	FP (%)	FN (%)	JS (%)
Elawady's method	53.86 ± 28.59	11.76 ± 33.10	46.14 ± 28.59	47.74 ± 26.65
Initial contour + CV	82.45 ± 5.33	2.28 ± 2.87	17.55 ± 5.33	79.72 ± 4.46
Initial contour + CV-ROEWA	85.52 ± 4.88	2.68 ± 3.11	14.48 ± 4.88	82.65 ± 3.58

Table 3

Segmentation performance measures of benign tumors

Methods	Accuracy (%)	Sensitivity (%)	Specificity (%)	PPV (%)	NPV (%)
Elawady's method	96.73 ± 2.88	70.39 ± 18.57	99.77 ± 0.40	96.97 ± 5.59	96.91 ± 3.24
Initial contour + CV	97.39 ± 2.03	84.92 ± 5.59	98.94 ± 1.50	90.89 ± 12.97	98.38 ± 1.65
Initial contour + CV-ROEWA	98.31 ± 1.50	87.84 ± 5.43	99.57 ± 0.54	96.79 ± 2.57	98.63 ± 1.55

Table 4

Segmentation performance measures of malignant tumors

Methods	Accuracy (%)	Sensitivity (%)	Specificity (%)	PPV (%)	NPV (%)
Elawady's method	87.89 ± 9.32	53.86 ± 28.59	96.62 ± 9.71	89.56 ± 23.13	90.39 ± 8.03
Initial contour + CV	95.40 ± 2.46	82.45 ± 5.33	98.98 ± 1.39	96.40 ± 4.29	95.92 ± 3.18
Initial contour + CV-ROEWA	95.96 ± 2.29	85.52 ± 4.88	99.05 ± 1.23	96.49 ± 3.90	96.49 ± 3.13

Table 5

A summary of the *p* values for accuracy, sensitivity, specificity, PPV, and NPV of Kruskal-Wallis test

Measurements	Accuracy	Sensitivity	Specificity	PPV	NPV
p	< 0.0001	< 0.0001	< 0.0001	0.0003	0.0002

Table 6

A summary of the p values of post hoc analysis (p_{12} is calculated between Elawady's method and the initial contour + CV model, p_{13} is calculated between Elawady's method and the initial contour + CV-ROEWA model, and p_{23} is calculated between the initial contour + CV model and the initial contour + CV-ROEWA model)

Measurements	Accuracy	Sensitivity	Specificity	PPV	NPV
p_{12}	0.0238	< 0.0001	< 0.0001	0.0005	0.0137
p_{13}	< 0.0001	< 0.0001	< 0.0001	0.0043	0.0002
p_{23}	0.2095	0.0529	0.9135	0.8155	0.4614

Table 7

Classification of breast tumors by SVM with morphological features

Methods	Correct	Accuracy (%)	AUC
Manual segmentation	17	85	0.94
Initial contour + CV	14	70	0.90
Initial contour + CV-ROEWA	18	90	0.94